ilmedia

Technische Universität Ilmenau

Wang, Anni; Gallino, Isabella; Riegler, Sascha Sebastian; Lin, Yi-Ting; Isaac, Nishchay A.; Sauni Camposano, Yesenia Haydee; Matthes, Sebastian; Flock, Dominik; Jacobs, Heiko O.; Yen, Hung-Wei; Schaaf, Peter:

Ultrafast formation of single phase B2 AlCoCrFeNi high entropy alloy films by reactive Ni/Al multilayers as heat source

Ultrafast formation of single phase B2 AlCoCrFeNi high entropy alloy films by reactive Ni/Al multilayers as heat source

Anni Wang [a,1], Isabella Gallino [b], Sascha Sebastian Riegler [b], Yi-Ting Lin [c], Nishchay A. Isaac [d], Yesenia Haydee Sauni Camposano [a], Sebastian Matthes [a], Dominik Flock [a], Heiko O. Jacobs [d], Hung-Wei Yen [c], Peter Schaaf [a,*]

[a] TU Ilmenau, Institute of Materials Science and Engineering, Institute of Micro and Nanotechnology MacroNano®, Chair Materials for Electrical Engineering and Electronics, Gustav-Kirchhoff-Str. 5, 98693 Ilmenau, Germany
[b] Saarland University, Chair of Metallic Materials, Campus C6.3, 66123 Saarbrücken, Germany
[c] Department of Materials Science and Engineering, National Taiwan University, No. 1, Sec. 4, Roosevelt Road, 10617 Taipei, Taiwan
[d] TU Ilmenau, Institute of Micro and Nanotechnology MacroNano®, Group Nanotechnology, Gustav-Kirchhoff-Strasse 1, 98693 Ilmenau, Germany

HIGHLIGHTS

- High entropy alloy films with single phase B2 AlCoCrFeNi fabricated from multilayers.
- Self-propagating combustion using Al/Ni multilayers is used as an ultrafast heat source.
- Fast scanning calorimetry reveals that the phase formation sequence depends on heating rate.
- High heating rates avoid long-range diffusion and intermediate phases.

GRAPHICAL ABSTRACT
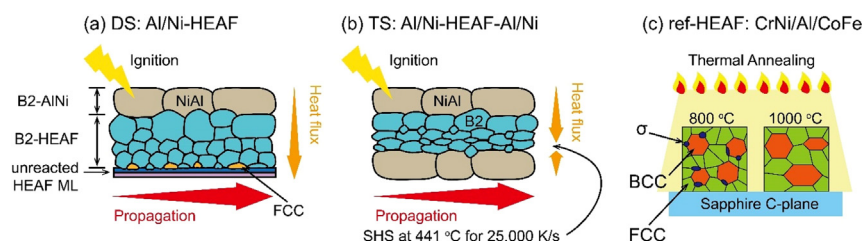
ABSTRACT

High entropy alloy films of AlCoCrFeNi B2-ordered structure are formed during an ultrafast heating process by reactive Ni/Al multilayers. The self-propagating high-temperature reaction occurring in reactive Ni/Al multilayers after ignition represents an ultrafast heat source which is used for the transformation of a thin films Al/CoFe/CrNi multilayer structure into a single-phase high entropy alloy film. The materials design of the combined multilayers thus determines the phase formation.

Conventional rapid thermal annealing transforms the multilayer into a film with multiple equilibrium phases. Ultrafast combustion synthesis produces films with ultrafine-grained single-phase B2-ordered compound alloy. The heating rates during the combustion synthesis are in the order of one million K/s, much higher than those of the rapid thermal annealing, which is about 7 K/s. The results are compared with differential scanning calorimetry experiments with heating rates ranging from about 100 K/s up to 25000 K/s. It is shown that the heating rate clearly determines the phase formation in the multilayers. The rapid kinetics of the combustion prevents long-range diffusion and promotes the run-away transformation. Thus, multilayer combustion synthesis using reactive Ni/Al multilayers as heat source represents a new pathway for the fabrication of single phase high-entropy alloy films.

1. Introduction

High entropy alloys (HEA) have attracted intensive research interest owing to their superior properties, for instance, an excel-

lent combination of high yield strength and ductility, good corrosion and oxidation resistance, retained mechanical strength at elevated-, cryogenic- temperatures, and radiation [1,2]. In contrast to conventional alloys, where one element acts as a solvent while the others act as solute elements, HEA are made of n constituents with equiatomic or close-to-equiatomic composition and $5 \leq n \leq 13$ [3]. This drastically increases the configurational entropy of the system and thus stabilize solid solution phases in the middle of the compositional range to form either simple centered cubic (FCC), body-centered cubic (BCC) or hexagonal close-packed (HCP) crystal structures. As for thin films and coatings, high entropy alloy films (HEAF) are considered to be ideal candidates as coating materials for extreme temperatures and aggressive environment applications, as they are also corrosion resistant and damage tolerant [4–7].

Various techniques have been used to deposit HEAF, including magnetron sputtering, laser cladding, spraying, electrodeposition, and plasma-transferred arc cladding [5]. A successful multilayer synthesis for MAX phase coatings and films by rapid thermal annealing was already reported [8–10]. More recently, multilayer synthesis using magnetron sputtering and subsequent heat treatment was proposed by Cai and co-workers. [11]. They observed the formation of a BCC/FCC dual phase composition in AlCoCrFeNi-based HEAFs with tunable mechanical performance up to 10 GPa in hardness. In contrast to bulk synthesis methods, which generally are performed above the elements' melting temperatures, i.e., for temperatures greater than 1000 °C [12,13], the synthesis parameters in sputtered multilayers can be significantly reduced down to 550 °C. In our latest investigation on CuCrCoFeNiO HEAF via multilayer alloy formation [14], we observe a further reduction of HEAF phase formation conditions at 600 °C for 5 min by introducing the nanoscale size effect on diffusion kinetics and phase equilibria.

In this work, we investigate a novel synthesis route to produce B2-HEAF that judiciously stacks together two nanocrystalline multilayered thin films that differ in nature and functionality, namely a highly reactive Ni/Al multilayer film (Ni/Al-unit) that acts as a fast heating source, and a CrNi/Al/CoFe multilayered film (HEAF-unit) that is transformed to HEA by the imposed heat and also acts as a heat sink. Our HEAF unit arranges a layer of pure Al in between layers of the equi-binary CrNi and CoFe alloys within the HEAF-unit, aiming for an enhancement of intermixing at interfaces based on the highly negative enthalpy of mixing values between Al and each of the other elements. A self-propagating high-temperature synthesis (SHS) reaction is ignited in the additionally deposited external Ni/Al-unit by an electrical discharge or induced by increased temperatures in fast scanning calorimetry (FSC). We have selected the highly reactive Ni-Al system for the Ni/Al-unit as heat source, using a small bilayer periodicity (60 nm) and a composition (60 at.% Ni) that lies in the NiAl-B2-range of stability [15]. According to the literature, the SHS reaction velocity in Ni/Al multilayer thin films is as fast as 5 m/s and the heat released by the formation of NiAl-B2 is in the order of −41 to −59 kJ/mol [15–24]. This large amount of heat release and the resulting temperature increase are used to induce a kinetic controlled non-equilibrium multilayer combustion synthesis within the HEAF-unit to form the B2-ordered structure via polymorphic transformation. The AlCoCrFeNi-system is selected as a model system due to the relatively complex equilibrium thermodynamics that involves the formation of more than one phase, depending on the synthesis temperature. According to the literature, isothermal annealing below 1123 K (850 °C) results in the formation of σ-phase intermetallic compounds embedded in a dual FCC/BCC matrix, whereas above 1123 K usually only the dual FCC/BCC phase is observed to form in a wide temperature range [25–27]. B2-structured phases in the equiatomic AlCoCrFeNi-system are known to be stable as

single-phase only at above 1663 K (1390 °C) close to the *liquidus* temperature [28]. The calculated enthalpy of formation for AlCoCrFeNi -B2 phase is moderately negative between −15.0 and −19.1 kJ/mol [29], thus it is expected to assist the SHS reaction by inducing some extra heat by local intermixing and reaction. This was proved here based on extensive microstructural, structural and calorimetric analyses.

2. Experimental procedures

2.1. As deposited material

The multilayer sequence of the HEAF-unit is [CrNi/Al/CoFe] and consists of a 16.5 nm layer of equiatomic CrNi, a 11.3 nm thick layer of pure Al, and a 20 nm thick layer of equiatomic CoFe. Within the HEAF unit, the layers of elemental Al are designed to have direct interface contacts with the binary alloys to ensure high negative enthalpy of mixing during the initial intermixing [29]. The HEAF-unit has a total thickness of 765 nm and contains 16 repetitions of the aforementioned tri-layer sequence.

The Ni/Al-unit has a total thickness of 720 nm and contains 12 Ni/Al bilayer repetitions with thicknesses of 30 nm Al and 30 nm Ni. The overall composition in the Ni/Al-unit is thus about $Al_{40}Ni_{60}$. Three planar multilayer composite designs are produced, namely a single-stack (ref-HEAF) bearing only the CrNi/Al/CoFe-multilayer sequence, a double-stack (DS) Ni/Al–CrNi/Al/CoFe, and a triple-stack (TS) Ni/Al– CrNi/Al/CoFe–Ni/Al, as shown in Figs. 1–2.

The DS- and TS-multilayer composites are deposited onto a Si (1 1 1) wafer using a dc-magnetron sputtering system (LA 440S, Ardenne), whereas the ref-HEAF multilayer is directly deposited onto a c-plane sapphire wafer. For both DS- and TS-morphologies the Ni/Al-unit is the first to be deposited. The interface between the Si-substrate and the Ni/Al-unit is a 50 nm wet-etched SiO_2. Four target materials are used: Al (99.99% purity, FHR), Ni (99.99% purity, FHR), CrNi (50:50 at.%, FHR), and CoFe (50:50 at. %, FHR). The individual layer thickness is controlled by adjusting the deposition time with a pre-calibrated deposition rate for each target (Al: 1.56 nm/s, Ni: 1.56 nm/s, CoFe: 1.78 nm/s, CrNi: 1.09 nm/s). The sputtering power was 200 W DC at a working pressure of 8.8×10^{-3} mbar with 80 cm³/min of argon flux. The HEAF-unit was deposited directly on top of the Ni/Al-unit. In the case of the TS, one additional Ni/Al-unit is deposited on top of the specimen. The final layer is a c-plane sapphire wafer. After deposition, free standing films are obtained by manually peeling off the films from the substrates, following the procedures developed in [30–33].

Fig. 1 shows the appearance of as-deposited DS and TS specimens after detachment from the $SiO_2/Si(1 1 1)$ substrate. The DS free-standing film in (a) rolls up due to high growth-in stress and intensive interfacial stresses in this complex multilayer system, which is a common feature of many multilayer systems [34]. In addition, the overall elastic mismatch between the Ni/Al unit and the HEAF-unit could also contribute to large bending stresses. In contrast to DS, the TS composite is a flat stress-free foil, as shown in the photograph in (b). The extra Ni/Al unit on top holds a counterbalance stress value that lowers the overall residual stress. Moreover, the sandwich-type morphology in the TS-composite provides additional support for structural integrity. However, an in-depth stress gradient is not neglectable, and the reaction thermodynamics and kinetics could be influenced by it.

2.2. Ignition methods

An electrical discharge of about 1 mA at 20 V is applied for the TS and DS free standing foils for ignition, and the reactions are
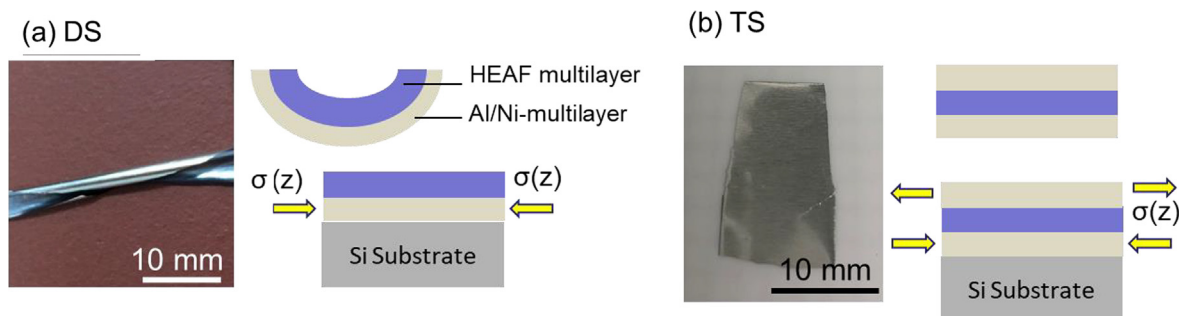
Fig. 1. Multilayer composites: (a) Double-stack (DS): Ni/Al-CrNi/Al/CoFe; (b) Triple-stack (TS): Ni/Al-CrNi/Al/CoFe-Ni/Al. The DS free-standing foil rolls up after peeling from the substrate because of the high residual stresses and the significant stress gradient σ(z) with depth. On the other hand, the flat TS free-standing foil indicates a balance of stress gradient σ(z) and low overall stress value ∑σ(z) due to the symmetry of the design.
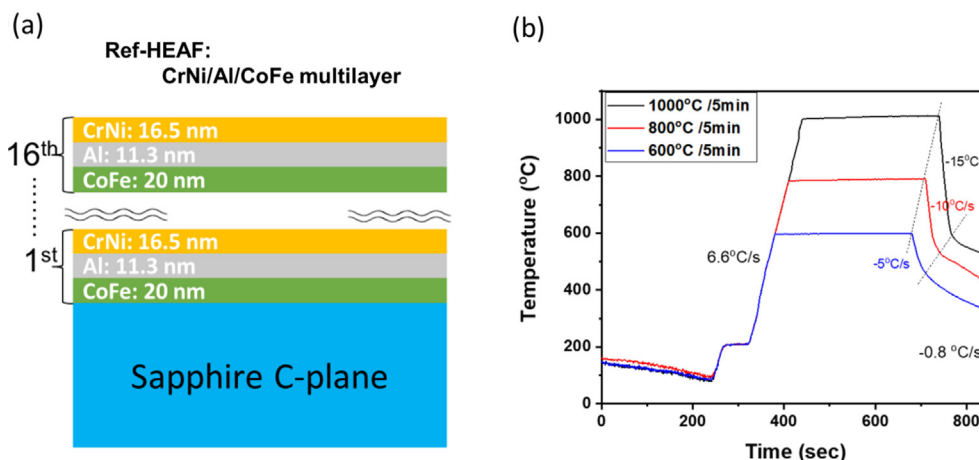

Fig. 2. Reference CrNi/Al/CoFe-multilayer (ref-HEAF): (a) Schematics of the deposition design onto a c-plane sapphire wafer. The layer compositions and individual layer thickness are labeled, and in total 16 repetitions were deposited. (b) Experimental temperature profile for the isothermal treatments in RTP at 873, 1073 and 1273 K (600, 800 and 1000 °C) respectively, for 5 min holding time.

recorded under a high-speed camera (MotionBLITZ EoSens mini1, Mikrotron) with a frame rate between 4.5×10^3 to 5.2×10^3 frame/s depending on the image size. We made sure that the electrical discharge is applied directly onto the Ni/Al-multilayer side for the ignition of the DS foils. No specific side was selected for TS, since this is a sandwich configuration and an Ni/Al-multilayer is located on each side. For a proper ignition, at least 5 mm × 10 mm of surface area was required for the electrical contact.

Fast scanning calorimetry (FSC) is performed with the TS-composite using the Flash DSC 2+ of Mettler Toledo based on a differential scanning chip-calorimetry technology. The calibration of the chip-sensor was ensured through the melting of standard pure elements as explained in ref. [35]. FSC specimens were obtained by manually cutting a free-standing film from a TS sample. Prior to the experiment, the actual mass of each FSC specimen was determined based on the imprinted geometry using experimental data for surface area. The surface area measurements are performed using the image software GIMP 2 on optical photographs acquired with a LEICA M60 optical microscope equipped with a LEICA IC 90 E camera. Each specimen is manually placed onto the active area of the sample-side of a high-temperature chip sensor. In order to enhance the signal to noise ratio, smaller specimens were used for faster applied heating rates, e.g., for a scan at 100 K/s approximately 100 ng of material is used and we gradually have reduced the specimen mass to approximately 10 ng, as we increased the heating rate to 25000 K/s. The FSC cell was constantly purged with argon gas at a rate of 20 ml/min prior to and throughout the measure-

ment. For each specimen a baseline is obtained by performing a second up-scan with the reacted material.

The ref-HEAF specimens were annealed for 5 min isothermally at 600, 800, and 1000 °C under a flow of an Ar/H₂ mixture by employing a rapid thermal process (RTP, Jetstar 100, Jipelec). Fig. 2 (b) shows the recorded temperature profile for each of these isothermal treatments. The applied heating rate to reach the isothermal temperature was 6.6 K/s and the cooling was a furnace cooling. The heating rate of the Ni/Al multilayer's self-propagating reaction is in the order of about 10^6 K/s with a maximum temperature in the range of 900–1100 °C according to own pyrometer measurements and the literature [16,24].

2.3. Characterization techniques

Structural, microstructural and chemical characterizations were performed using a combination of methods, namely using an X-ray diffractometer (XRD, Siemens D5000), a scanning electron microscopy- focused ion beam system (SEM-FIB, Zeiss Auriga 60) equipped with an energy-dispersive X-ray Analysis (EDX). Morphologies of the as-deposited and reacted specimens were observed by employing SEM, and the element distribution was measured using EDX mapping at a magnification of 2×10^4. The overall elemental ratio of AlCoCrFeNi was determined by EDX mapping on the as-deposited ref-HEAF. Cross-sectional images were accomplished in a dual-beam SEM/FIB system to observe the microstructural evolution concerning different thermal treat-

ments on ref-HEAF in comparison with those of the spark ignited specimens DS and TS. The HEA phase formation was observed using X-ray diffractometer (XRD, Siemens D5000) operated at 40 kV and 40 mA with Cu-Kα X-ray source (λ = 1.5405 Å) in Bragg-Brentano θ-2θ geometry. The free-standing DS and TS samples were placed on top of quartz glass and secured to the sample stage. The diffractometer was under parallel-beam configuration with a line focus, where the size of the beam-defining collimating slit was 1 mm. 2θ-scans ranged from 20° to 100°, and a sampling step of 0.02° and a rate of 1.2°/min were employed. The identification of the crystalline phases was conducted using DIFFRAC. EVA V5.1 and Peakfit V4.2 software and coupled with the powder diffraction files (PDF) database [36]. The peak positions were determined by employing pseudo-Voigt functions and were used to calculate lattice parameters and crystalline volume fractions [37]. Transmission Kikuchi diffraction (TKD) was applied on TS and DS laminar samples to resolve the composition, morphology, and crystalline structure of the AlCoCrFeNi coating in comparison with those of annealed ref-HEAF. The annealed ref-HEAFs are named after the annealing condition: ref-600 °C/5min, ref-800 °C/5min and ref-100 °C/5min.

Microstructure constituents and crystallography of the ignited specimens were investigated by using transmission Kikuchi diffraction (TKD) in a JEOL JSM-7800f Prime field emission gun scanning electron microscope (SEM) equipped with a NordlysNano EBSD detector. The experimental setup of TKD analysis were done under an acceleration voltage of 30 kV and step size of 8 nm [38]. Coupled with TKD experiments, the chemical compositions were simultaneously mapped with the X-MaxN detector for the X-ray energy-dispersive spectroscopy (EDS). Supplementary on-site diffraction patterns were obtained by electron diffractions in a FEI Tecnai G2 F20 transmission electron microscopy (TEM). TKD and TEM investigations were done on cross-sections and the specimens were prepared by a dual-beam focused ion beam (FIB) system (Helios Nanolab 600i, FEI). The surface was initially deposited with platinum to avoid specimen damage during FIB milling. The final thickness of FIB specimens was about 100 nm.

3. Results

3.1. Combustion studies

After electrical discharge ignition, the surface topography of DS and TS composites were observed using SEM, and the results are reported in the microphotographs of Fig. 3.

Depending on the stacking sequence, different surface topological features are observed. The surface of a reacted DS composite (a-b), from the HEAF-side, show periodic ripples that spread from the initial ignition point. At large magnification (c-d), the surface appears smooth and featureless. These ripples indicate an unstable propagation front similar to the one observed in several other reactive multilayers [16,39]. The extensive buckling of the DS foil, shown in Fig. 1 (a), together with a film thickness of only ~1.5 μm and the limited amount of surface area of about 5 × 5 mm^2, technically hindered high-speed video filming during combustion due to the limitation of the frame rate. The topological features of a reacted TS foil are shown in Fig. 3(e-i) and consists of a wide-scale of wavy structures ranging from mm down to μm in size. A curtain-like structure advances along the propagation direction (e), and repetitive wavy structural networks are observed within the folding sections (f). At larger magnifications (g-i), highly ordered curly noodle-like microstructures are observed within the wavy networks. Moreover, these features follow the reaction direction.

The combustion of the TS foil shown in Fig. 3(e-i) was filmed with the high-speed camera and labeled as Test A. In Fig. 4(a) we

report the time-lapse plan view video-photographs of this Test A, where a serrated reaction front is observed with an interval of 0.4 mm between the drapery folds-like features. It appears that the topological features that we observe in SEM in Fig. 3 are formed during the cooling process behind the reaction front and that the drapery folds-like features follow the reaction propagation direction. Based on the high-speed video results, the reaction front velocity differs locally. In Test A, along the fold ridges the reaction front average velocity was calculated as (3.35 ± 0.21) m/s, which is slightly faster than along the fold valleys, i.e., (3.29 ± 0.20) m/s.

The overall displacement of the reaction front during Test A is plotted as a function of time in Fig. 4 (b). We observe a bimodal propagation trend, made of a faster linear behavior (regime I) that holds as long as there is approximately still at least 15% of unreacted material ahead of the front. Also, in the other two ignition tests (B, C) of Fig. 4(b), there is the same apparent slowdown in the propagation mode of the reaction front at longer times (regime II). This is an indication that there must be a critical volume of unreacted material that is necessary ahead of the front in order for the reaction to be self-sustainable. Behind this threshold, the reaction apparently slows down until the reactants are completely consumed. The resulting overall velocities of the two additional ignition experiments B and C are somewhat faster than that of Test A. The fastest velocity is recorded during test C, i.e., (5.5 ± 0.2) m/s, which is as fast as SHS reactions observed with pure Ni/Al-multilayers [21]. The large scatter in reaction velocities in Fig. 4 (b) can be attributed to several factors playing simultaneously. One of these factors is the actual length of the foil. In fact, we have qualitatively observed that larger sample size specimens resulted in slower reaction speeds. Another factor influencing the reaction front velocity is the amount of structural damage and internal stresses that were induced into the material during the manual detachment from their substrate. Another observation that we have made is that the wavy reaction front that protrudes out of the sample surface may influence the length measurement of the high-speed camera investigation, each time differently.

Fig. 5 reports upon the FSC study performed with the TS-multilayer composite. Fig. 5(a) shows a selection of baseline-subtracted heat flow scans obtained for various applied heating rates, β. Upon scanning with heating rates up to 10000 K/s, the reaction follows a multistep reaction mechanism. The overall reaction in each scan ranges across more than 300 K from the onset- to the end-temperature (see Table 1). In contrast, when flash rates are applied ($\beta \geq 25000$ K/s), a change in the reaction mechanism is observed. In this case, the signal is very sharp, indicating a SHS mechanism. This reaction occurs completely in the solid-state at a critical ignition temperature of T_{onset} = 678 K, and it gets consumed in only 90 K from the ignition temperature, reflecting the explosive nature (runaway) of the thermal reaction. In Fig. 5(b), we have applied the Kissinger kinetic analysis method [40] to obtain an activation energy for each individual peak, where T_p is the peak temperature, β is the applied heating rate, and Q is the activation energy obtained from the slope value of the linear fit to the data (circles). In Fig. 5(b), we have added the peak temperatures for peak I and II, but did not use them in the fitting procedure. These values (black triangles) agree with the extrapolation of the Kissinger equation for the first peak (see dashed line). It has to be noted that the FSC allowed the Kissinger analysis to be performed in a range of more than 5 orders of magnitude in terms of $\ln(\beta/T_p^2)$ using a single device, which is twice as much as usually measured with conventional DSC, as for example in refs. [17,41].

3.2. Microstructural investigations

TKD analyses of TS- and DS-multilayer composites after spark-ignition are shown in Fig. 6 and Fig. 7, respectively.
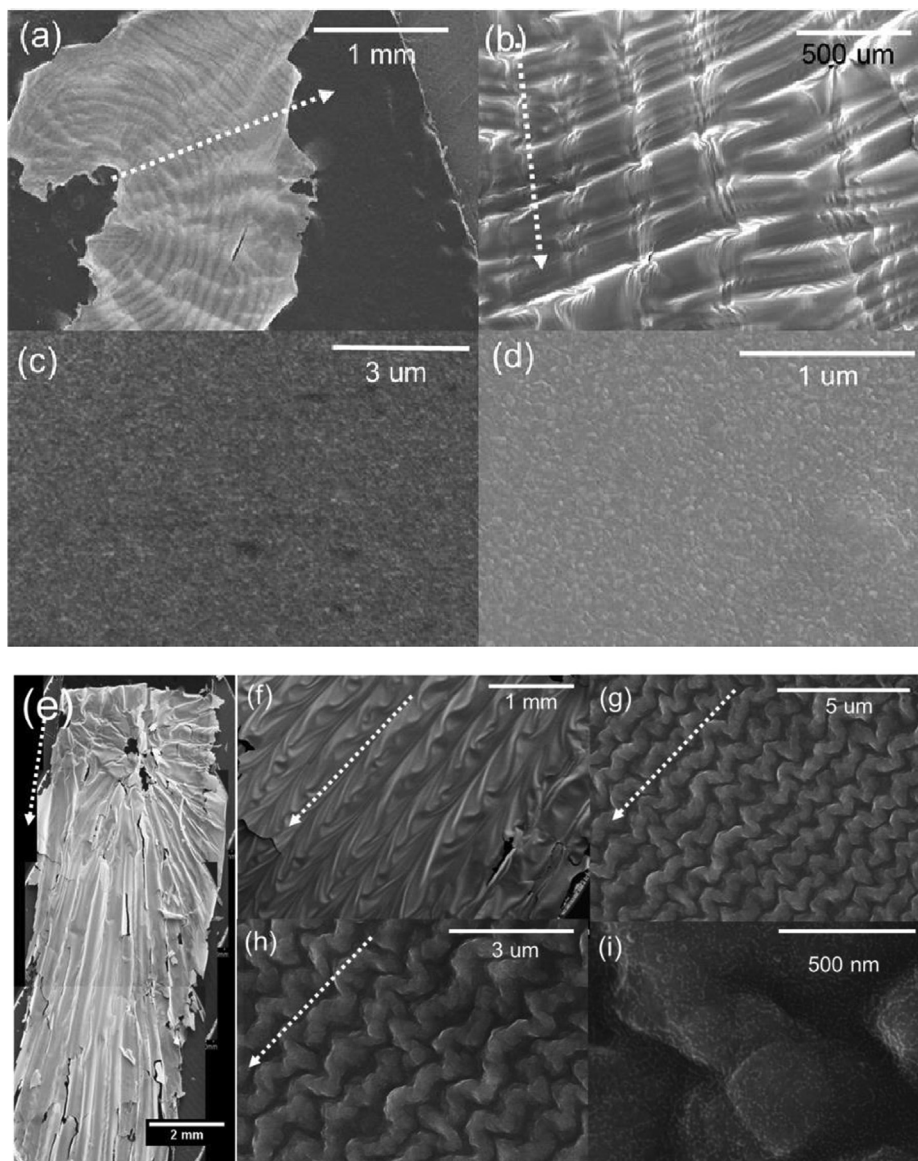
Fig. 3. SEM images of surface of reacted samples after electrical discharge ignition. (a–d) DS-composite Ni/Al-CrNi/Al/CoFe and (e-i) TS-composite Ni/Al-CrNi/Al/CoFe-Ni/Al. Arrows mark the propagation direction of the reaction front.

Overall, both samples show large gradients of grain size along the normal direction of surface, and no laminate structure from the as-deposited state is observed (an example is shown later). Novelties of their ultrafine-grained microstructure are detailed in the following. The microstructure in the reacted TS sample is pure B2-phase as seen in Fig. 6(a). The corresponding inverse pole figure of Y direction (IPF-Y and Y ∥ surface normal) is shown in Fig. 6(b). Texture of ⟨110⟩ ∥ surface normal is strong in the HEAF-unit and the bottom NiAl-unit, where the textured grains occupied at least 50 area% of the investigated region. Such strong texture is governed by the surface energy of B2 structure, where (110) surface has the lowest surface energy [42]. The upmost NiAl-unit could subject to template effect from the HEAF-unit that impacts the crystalline orientation. Actually, it is difficult to distinguish B2 from BCC by using TKD. On-site TEM diffraction patterns were done for one NiAl grain and one HEA grain as marked by (c) and (d), respectively, in Fig. 6(b). Both NiAl grain-(c) and HEA grain-(d) are B2 structures as proven in Fig. 6(c) and 6(d), respectively. The thickness of the NiAl grains is restricted by the initial thickness of deposited layers and the lateral size is about 773 nm. The thick-

ness of the larger HEA grains is about 203 nm and the lateral grain size is about 493 nm. Besides, there are some equiaxed HEA grains with size about 183 nm. As shown in Fig. 6(e)-6(i), HEA layer contains Al, Ni, Co, Cr and Fe and their distributions are uniform. Al and Ni tend to partition toward NiAl layers whereas Cr and Fe tend to partition toward HEA layer. However, in the TS sample, very limited interdiffusion was observed. This could be due to sluggish diffusion of the HEA phase and limited diffusion kinetic under rapid thermal conditions. Furthermore, the interface boundary complexion between binary and multicomponent alloys should be considered [43], where the misfit strain and possible reduced interfacial energy could as well reduce the boundary mobility. Since the interdiffusion between the NiAl- and the HEAF-layers is limited, it is thus reasonable to consider that the formation of the HEA phase in TS is solely due to the combustion synthesis process.

In the DS sample, the primary microstructure is the B2-phase and, interestingly, several tiny FCC grains can be observed on the surface as seen in Fig. 7(a). As displayed in Fig. 7(b), in the HEAF-unit, B2 grains show very strong texture of ⟨110⟩ ∥ surface normal and FCC grains show strong texture of ⟨111⟩ ∥ surface normal.
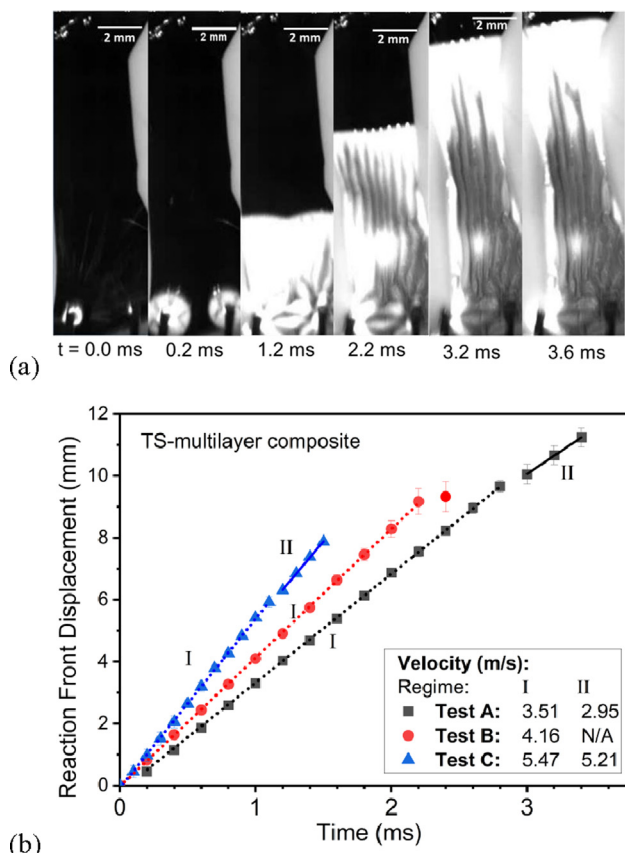
(a)

(b)

Fig. 4. High-speed camera test results for the TS-composite. (a) Time-lapse plan-view images of Test A at selected reaction times as indicated from 0.0 to 3.6 ms. (b) Plot of the propagation of front displacement versus time for all 3 individual ignition tests. Symbols represent the average data points from individual high-speed camera images. The lines are linear fits to the data within the indicated kinetic regimes (I – dotted and II - solid). The velocity of the reaction front is calculated from the slope of the linear fits, which ranges from (3.5 ± 0.2) m/s up to (5.5 ± 0.2) m/s in regime I.

On-site TEM diffraction patterns were done for one B2 grain and one FCC grain in the HEAF-unit as marked in Fig. 7(b). These characterizations are consistent with TKD analysis as seen in Fig. 7(c) and 7(d). Again, thickness of NiAl grains is restricted by initial thickness of deposition and lateral size of about 990 nm. In the interdiffusion layer, there are B2-structured grain with size about 277 nm and they have no preferred orientation. HEA grains beneath the surface are equiaxed and the size is about 162 nm. As shown in Fig. 7(e)-7(i), lamella distributions of Al, Ni, Co, Cr and Fe in the HEA layer beneath the surface can be observed. This phenomenon is not seen in the TS sample. Hence, in the HEAF-unit, the microstructure is made of equiaxed polycrystalline grains. EDS shows that still some finer contrast in the elemental maps exist, resembling a lamellar structure. Moreover, elemental distributions are inhomogeneous where the Ni and Al are more prominent towards the NiAl films, whereas Cr and Fe tend to partition more away from the NiAl film, maybe originating from an interdiffusion layer between NiAl and HEAF. In the DS sample, the interdiffusion layer is as thick as about 500 nm, which is much thicker than the case in the TS sample. These inhomogeneous chemical distributions indicate insufficient mass transportation and thus lacking the necessary configurational entropy effect in this system. Based on this, the HEAF phase formation in the DS-composite is questionable, and if any, it can only be described as a transition state. Interestingly, despite the considerable compositional gradient in the HEAF-unit, the HEAF grains within still hold a significant texture of ⟨1 1 1⟩, which could be due to pre-existed texture at the as-deposited state that was observed in our previous investigation on Cu/CrNiO/FeCo multilayers [14]. Following the concentration gradient (Fig. 7 (e)-(i)) and structural changes (Fig. 7 (a)) in DS from the NiAl-side outward, it is clear that the elements mixing, phase transformation, and grain growth are initiated by the Ni/Al multi-layer exothermic reaction. Hence, thermal energy and its gradient should be the primary driving force for this combustion method on the HEAF layer. Comparing the asymmetrical (DS) and symmetrical (TS) multilayer designs, the TS composite has a uniform and sufficient heat transfer to promote elemental intermixing and full phase transformation, whereas in the DS-composite the transformation seems not fully complete.
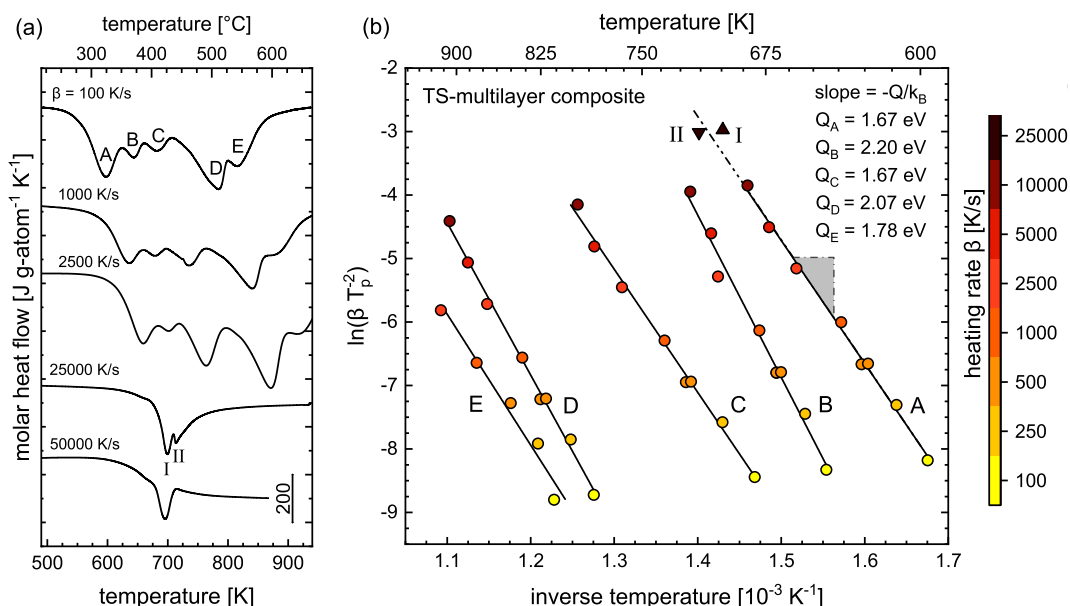

Fig. 5. Fast scanning calorimetry (FSC) results of the TS-multilayer composite (Ni/Al-CrNi/Al/CoFe-Ni/Al). a) Selected scans at the indicated heating rate from β = 100 K/s up to 50000 K/s. The low heating rates give rise to five exothermal peaks (A-E) and an overall enthalpy of reaction, ΔH = (−61.3 ± 11.1) kJ/mol, whereas the signals at flash rates of 25000 K/s or higher show only a sharp double-peak exothermic event (I and II) and a ΔH of (−15.0 ± 2.7) kJ/mol. b) Activation energy plot for Peak A through E following the Kissinger kinetics analysis. Q is the activation energy and k_B is the Boltzmann constant.

Table 1
Characteristic temperatures, heats of reaction and activation energies measured in FSC for the TS-composite.

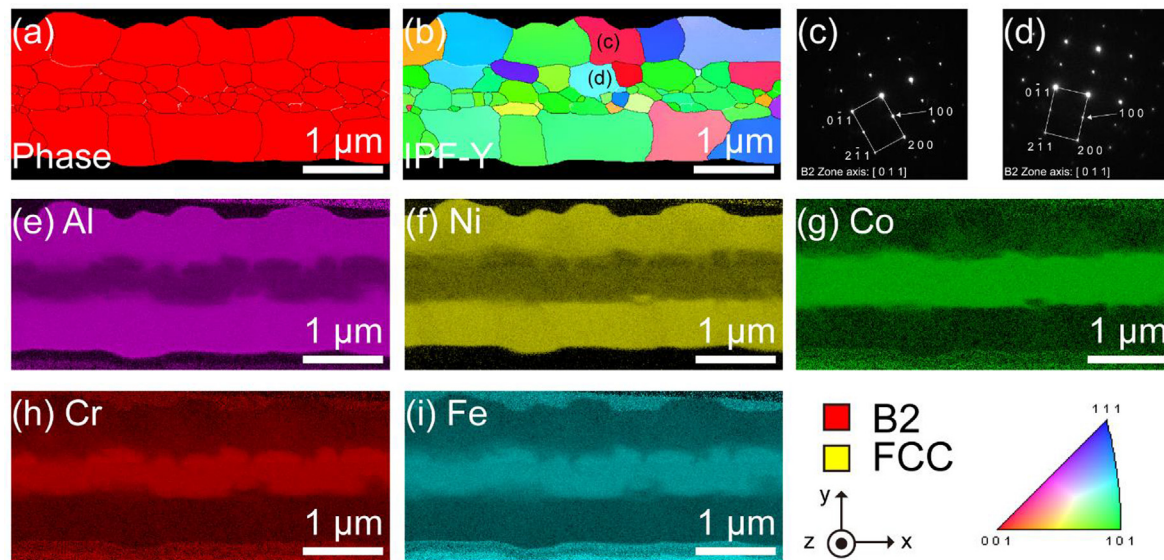|	ΔH [kJ/mol]	T_{onset} [K]	T_{end} [K]	T_{peak} [K]				
FSC at 100 K/s:	−61.3 ± 11.1	550	863	T_A: 598	T_B: 645	T_C: 683	T_D:785	T_E:817
FSC at 25000 K/s:	−15.0 ± 2.7	678	768	T_I: 700			T_{II}: 714	
Activation energy Q [eV]	Q_A: 1.67 ± 0.04		Q_B: 2.20 ± 0.10		Q_C: 1.67 ± 0.05		Q_D: 2.07 ± 0.06	Q_E: 1.78 ± 0.23

Fig. 6. TKD-EDS coupled analysis of a reacted TS-multilayer composite Ni/Al-CrNi/Al/CoFe-Ni/Al after spark-ignition: (a) phase map, (b) IPF-Y (IPF-Y and Y ‖ surface normal), (c) electron diffraction pattern of the B2-structure of a NiAl grain, (d) electron diffraction pattern of the B2-structure of HEA grain, and (e)-(i) X-ray EDS mapping of Al, Ni, Co, Cr and Fe.
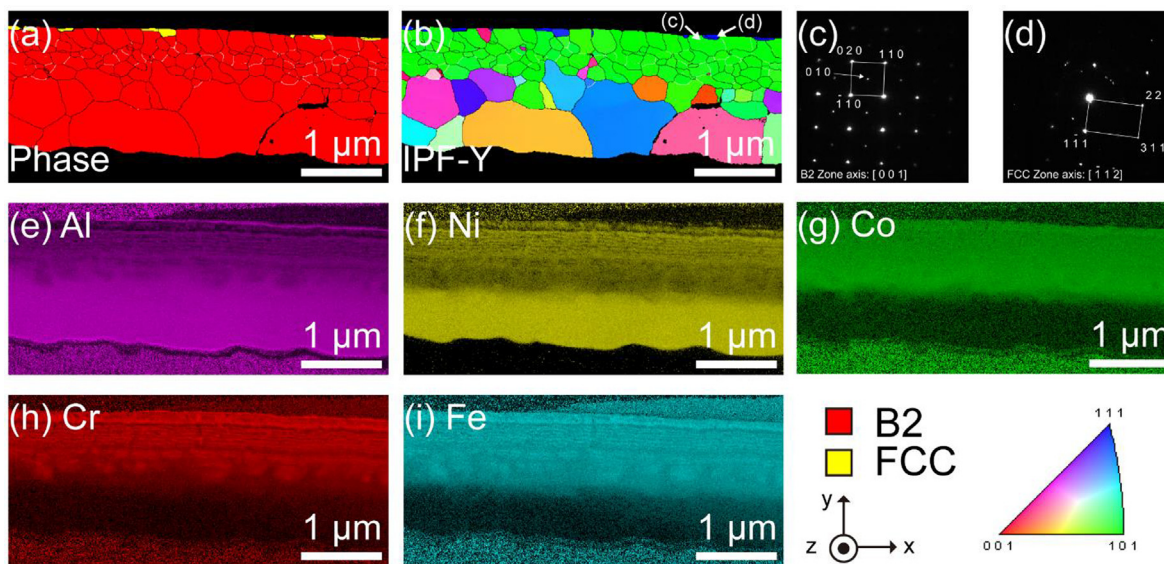

Fig. 7. TKD-EDS coupled analysis of a reacted DS-multilayer composite Ni/Al-CrNi/Al/CoFe after spark-ignition: (a) phase map, (b) IPF-Y, (c) electron diffraction pattern of B2-structure, (d) electron diffraction pattern of FCC structure and (e)-(i) X-ray EDS mapping of Al, Ni, Co, Cr and Fe.

In the following, we compare our novel HEAF synthesis route that uses reactive Ni/Al multilayers as a heat source with that of a reference material consisting only of the CrNi/Al/CoFe multilayered morphology (ref-HEAF). Fig. 8 reports the XRD result of the TS-composite and the ref-HEAF, in (a) and in (b), respectively. Composition distribution and microstructure of the ref-HEAF are carried out via SEM-EDX, and shown in Figs. 9 and 10. For the TS-composite in as-deposited conditions, the reflections of Al (1 1 1) at 38.5° and a combination of Cr(1 1 0), Ni(1 1 1) and CoFe (1 1 0) reflections at 44.5° are observed in Fig. 8(a). After electrical ignition, the Al reflections disappeared, and instead reflections that can be associated to an ordered B2 structure are visible, where the most intense reflection at 31.1° can be assigned to the B2 (1 0 0) reflection. A pure B2 structure is thus observed for the reacted
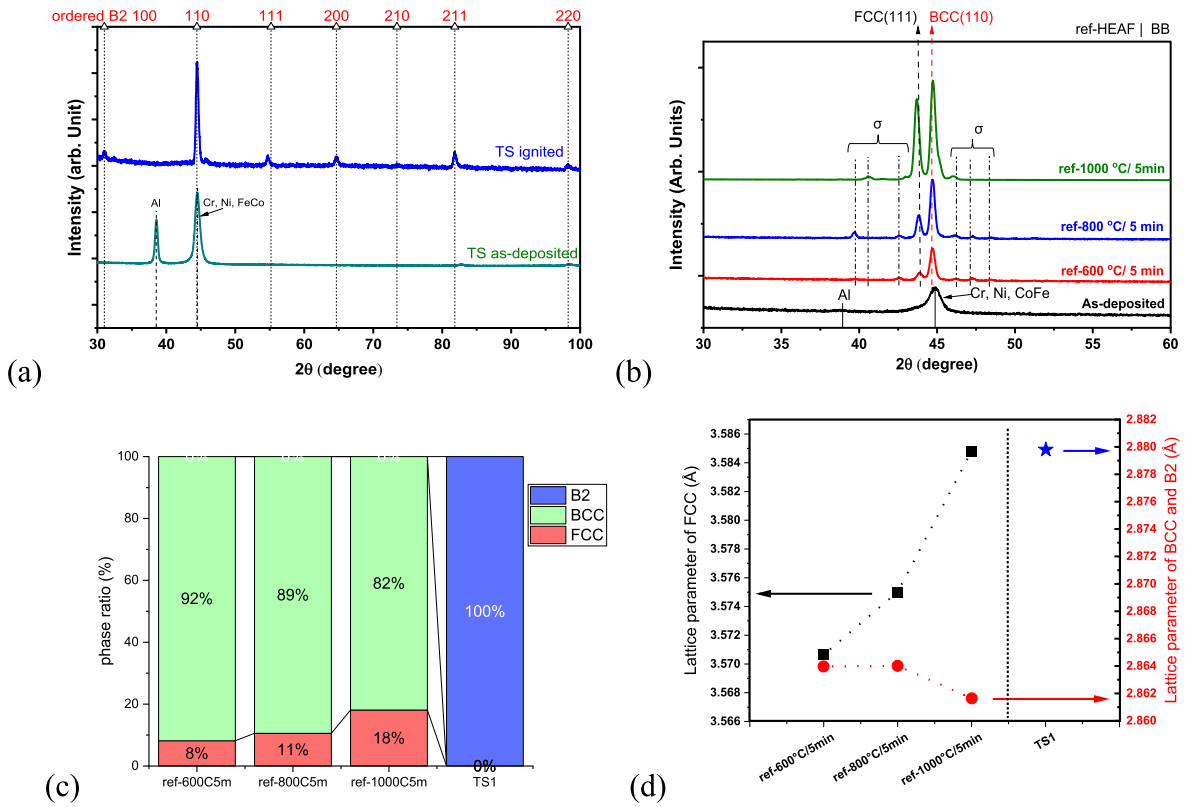
Fig. 8. XRD diffraction results. (a) Patterns of the TS-composite, before and after ignition. (b) patterns of the ref-HEA, before and after annealing. (c) Volume ratio values for the ref-HEAF taken from panels (a,b) for the ref-HEAF and from Fig. 6(a) for the TS-composite. (d) Lattice parameters of B2, BCC and FCC structures of the spark-ignited TS-composite (blue star) and annealed ref-HEAF (red circles and black square), respectively. (For interpretation of the references to colour in this figure legend, the reader is referred to the web version of this article.)
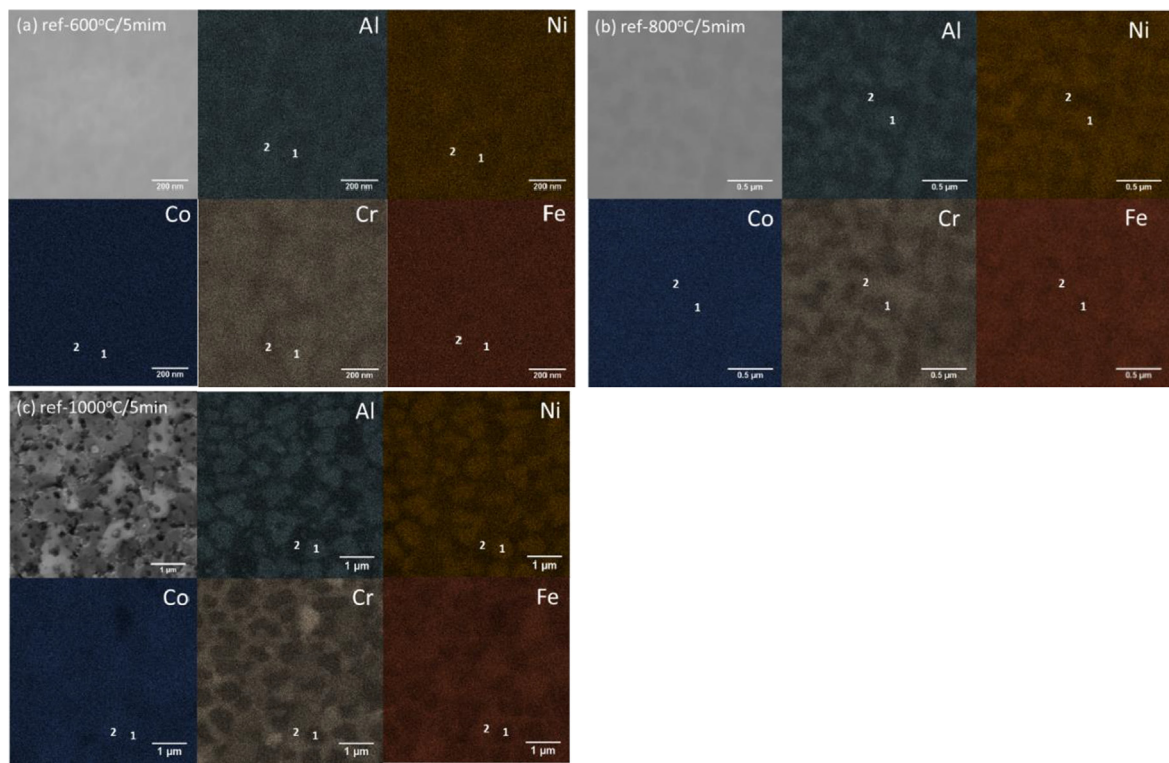

Fig. 9. EDX mapping of ref-HEAF (CrNi/Al/CoFe-multilayer) after isothermal annealing (a) ref-600 °C/5min, (b) ref-800 °C/5min, and (c) ref-1000 °C/5min. The labels 1 and 2 indicate where selected point analyses where performed for the study of Ni-Al-rich and Cr-Fe-rich domains (see Table 2).
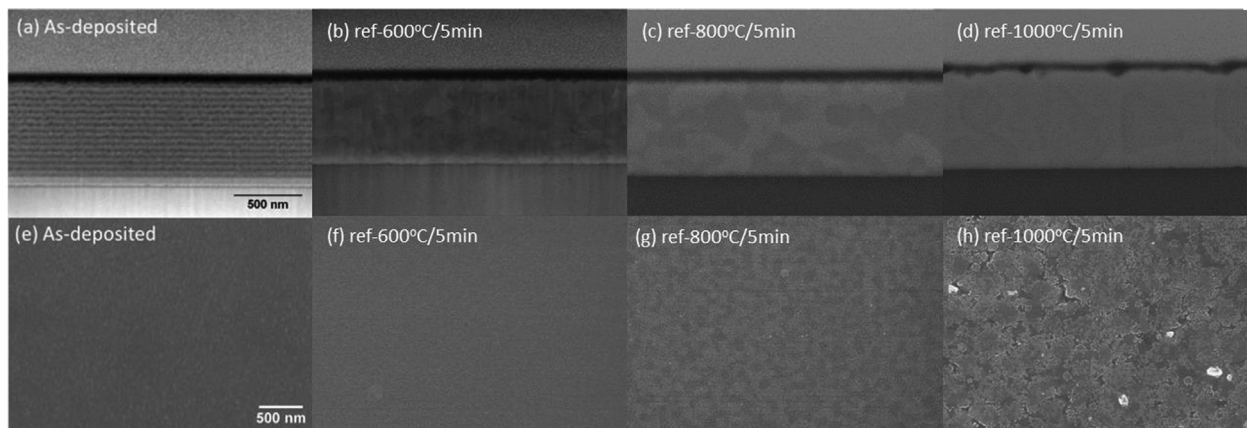
Fig. 10. SEM micrographs of ref-HEAF (CrNi/Al/CoFe-multilayer). (a-d) Cross sections. (e-h) Top view images. The specimens in (a, e) are in as deposited conditions. The other images correspond to specimens after the indicated heat treatments.

TS-composite. In fact, reflections associated to any other crystalline intermetallic compounds are completely absent here. This result agrees with the TKD phase maps in Figs. 6-7. Because the lattice parameter in AlCoCrFeNi is close to that of NiAl, most XRD reflections have slightly asymmetrical shapes, show a shift in peak position and peak-broadening.

In Fig. 8(b), the ref-HEAF before and after RTP annealing at 600, 800, and 1000 °C for 5 min are shown. A similar investigation and synthesis procedure can be seen in a previous publication [14]. After annealing, three phases are observed, including FCC, BCC, and σ. Because of the strong texture orientation, only a 30 to 60° scan is reported here. The B2 phase can be excluded, based on the absence of the (1 0 0) reflection at 31.1°. The σ phase is an intermetallic phase of a body centered tetragonal P42/mmm structure, and it is commonly found in AlCoCrFeNi at a synthesis temperature between 873 and 1273 K [26,44]. The phase formation in our ref-HEAF specimen is in good agreement with literature experimental results [26,27,45].

The volume ratios of FCC and BCC are determined based on the intensity of each peak and the corresponding multiplicity, Lorentz-polarization and structure factors for FCC(1 1 1) and BCC(1 1 0) [37]; while the volume ratio of B2 structure for TS was taken from the TKD results in Fig. 6(a). Lattice parameters are calculated by employing the peak position in Fig. 8(a, b). It should be informed that the lattice parameter of the B2 phase is a combination of NiAl and AlCoCrFeNi phases, and this value is merely an approximation. Results are shown in Fig. 8(c) and (d) for phase ratio and lattice parameter, respectively. A temperature dependency of phase ratio is observed in ref-HEAF. The FCC volume ratio increases with the incline of lattice parameters, whereas BCC is on the contrary.

The lattice parameters change in FCC and BCC phase observed from XRD are primarily due to the element segregation in forming Ni-Al rich BCC phase and Fe-Cr rich FCC phase, as shown in EDX mapping in Fig. 9 and Table 2.

The microstructure of the ref-HEAFs before and after annealing are shown in Fig. 10, where the grain sizes increase as the temperatures increase from 600 to 1000 °C. Both, the 600 °C and 800 °C annealed samples show a homogenous granular distribution. 1000 °C samples possess elongated grains that occupy the whole film thickness, and grain boundary grooves are found on the surface, which is akin to TS samples in Fig. 6 (a). Nevertheless, these observations indicate an unstable phase separation in AlCoCrFeNi HEAF.

4. Discussion

Comparing ref-HEAFs after annealing with a dual FCC/BCC phase and TS sample with 100% pure B2 phase (see Fig. 8(c)), these differences in HEA phase transformation are heavily determined by the synthesis routes, heating rates and temperature. A pure B2-AlCoCrFeNi without the presence of small amounts of FCC and intermetallic σ phases are rarely found, and coexistence of FCC, BCC, and σ phases are mostly observed [3,7,25–27,46]. For equiatomic AlCoCrFeNi, the B2 structure is a high-temperature stabilized phase in a narrow temperature range from 1663 K to 1683 K (1390 °C to 1410 °C), according to CALPHAD phase calculations in [27,28]. For multilayer synthesis, diffusion kinetics is acknowledged to control the phase formation, and metastable phases are commonly found [47]. Although the kinetic impact on reactive multilayer HEAF has not yet been quantitatively investigated, several investigations [37,48,49] of bulk synthesis of CoCrFeNi-based HEAs have shown highly metastable kinetic-controlled phase transformations. In He's work on CoCrFeNiTi$_{0.4}$ [49], the formation of the intermetallic compounds, i.e., σ, γ', and R phase, was kinetically suppressed by rapid solidification, which is similar to our results on the TS-composite. In addition, the accelerated diffusions along grain boundaries could also assist the formation of B2 phase as observed by Tang and his co-workers [48], where the annealing-induced HEA formation depends on the difference in elemental diffusivity at the grain boundaries. Similar phenomena are also observed in Fig. 6 on TS. The selective diffusion of Al, Ni, and Co in Fig. 6 can be regarded as an anisotropy in terms of segregation at the interfaces [50]; and this kind of phenomenon is heavily guided by thermodynamic quantities such as enthalpy and entropy. Among the binary mixing of enthalpies in the AlCoCrFeNi HEA, Ni-Al, and Al-Co are of the highest.

We discuss in the following each of the two exothermic reaction evolutions observed in the calorimetric analysis of Fig. 5. Based on literature results and our own activation energy plot of Fig. 5(b), we can make some suggestions regarding the phase sequence. The first 3 peaks (A-C) resemble those that are commonly found during slow annealing in Ni/Al multilayered thin films and thus appear to be associated with the formation of equilibrium intermetallic compounds, which typically are Al$_3$Ni followed by Al$_3$Ni$_2$ and NiAl [41,51]. We cannot exclude in the early stage of the reaction a suppression of the Al$_3$Ni phase and, instead, the nucleation and grow of metastable intermediate phases, as typically found in sputtered multilayered aluminide thin films with small bilayer spacing [21,23,52]. The nucleation and growth mechanism of Al$_9$-Ni$_2$ along the interfaces presumably dominates in the early stage of the reaction (Peak A) as a consequence of the asymmetric diffusion of Ni into the Al. In fact, the activation energy value for Peak A is Q$_A$= (1.67 ± 0.04) eV, which agrees with the kinetic analysis for the Al$_9$Ni$_2$ phase for pure Ni/Al multilayers with similar bilayer

Table 2
Composition of ref-HEAF samples before and after annealing. Position 1 and 2 are taken from Fig. 9.

Sample		Element (at %) Al	Element (at %) Cr	Element (at %) Co	Element (at %) Fe	Element (at %) Ni
As-deposited	Overall	20.83	22.04	19.27	20.27	17.60
After 600 °C/5min	Overall	20.15	22.69	19.09	20.2	17.87
	Position 1	26.18	21.45	17.61	18.83	15.93
	Position 2	28.87	18.53	17.48	17.54	17.58
After 800 °C/5min	Overall	20.28	22.49	18.71	20.21	18.15
	Position 1	29.15	16.20	18.25	16.76	19.63
	Position 2	24.33	20.87	18.82	19.23	16.74
After 1000 °C/5min	Overall	19.69	21.29	20.07	21.12	17.83
	Position 1	29.15	15.94	18.48	16.59	19.84
	Position 2	20.29	20.14	20.61	22.78	16.18

spacing [17]. The last two reactions (D and E) appear to be associated to the internal multilayer combustion synthesis of the HEAF. In agreement with the new thermodynamic description of Stryzhyboroda and co-workers [28], these two peaks (D and E) should correspond to the solid-state transformation of the dual-phase BCC-B2 + σ. It is important to note that the onset-temperature for this reaction is found at a relative low temperature in the solid-state (see Table 1), which is characteristic for nanocrystalline structures with layer periodicity below 100 nm [22,52]. By integrating the overall FSC exothermic signal at 100 K/s of Fig. 5, the overall enthalpy released due to the solid-state reaction in the TS-composite is (-1276 ± 232) J/g. Similar values are obtained when we integrate the other scans at faster rates (up to 10000 K/s). This value corresponds to (-61.3 ± 11.1) kJ/mol, using 48.03 g/mol as molecular weight for the TS-specimen with an overall composition $Ni_{45}Al_{32}Cr_7Co_8Fe_8$ at.%. The large error results mainly from the estimation of the specimen mass and from the peak integration analysis, however the average value agrees with the sum of the heats for the formation of NiAl-B2 and AlCoCrFeNi-B2. In fact, if we consider the assessment of calorimetric data performed by Rzyman and Moser on the Ni-Al system [15], the NiAl-B2 phase has an extensive homogeneity range between 42 and 69 at.% Ni and for the present Ni/Al multilayer composition (60 at.% Ni), at the temperature where Al is in the molten state, the enthalpy of formation (ΔH_f) for the B2 phase is -55.1 kJ/mol. This is reduced with respect to that of the 50 at.% Ni composition due to the linear decrease of ΔH_f when leaving the equimolar composition because of an increase in disordering in the alloys. In addition, this value is expected to be less negative if the reaction takes place in the solid-state, as in this case. According to experimental data of ref. [53] and calculated values of ref. [54], the reduction in ΔH_f is about 7 kJ/mol, which makes ΔH_f for the NiAl-B2 in our Ni/Al-unit to be about -48 kJ/mol. Similar consideration can be made for the formation of the B2-AlCoCrFeNi phase in our HEAF-unit. According to ref. [29], we expect approximately for the HEA-B2 formation a $\Delta H_f = -15$ kJ/mol. The sum of the ΔH_f value for the HEA-B2 formation (-15 kJ/mol) with the one expected for the NiAl-B2 formation (-48 kJ/mol) is -63 kJ/mol, which agrees well with our measured value (-61.3 kJ/mol).

The most important novelty of the FSC study lies in the observation that when ultrafast heating rates are applied the reaction mechanism resembles that of a run-away synthesis or SHS, where the formation of the intermediate equilibrium intermetallic phases is kinetically suppressed and presumably the B2 phase is selectively formed, in agreement with the observations of refs. [24,55–58] made with other multilayered systems. In this work, we are able to experimentally observe for the first time a gradual kinetic destabilization of the intermediate phases and, in turn a gradual stabilization of the final phase. In fact, in the FSC scans of Fig. 5a, there is an evident increase of the magnitude of Peak C with respect to Peak A and B with increasing heating rate. The use of the FSC has allowed us also to assess the critical heating rate to by-pass the crystallization temperature of the intermediate phases, which is for this particular system between 10000 K/s and 25000 K/s.

The combination of FSC results of Fig. 5 with the structural information of Figs. 6 and 7 points towards a reaction of the multilayer composite as a whole into the respective B2-structures. This observation agrees with the concept that ultrafast heating rates do not allow time for the long-range diffusion that is needed for non-polymorphous nucleation and agrees with the simulations of ref. [59] and with ref. [29]. Therefore, Peak I in Fig. 5 seems to be associated to the direct nucleation of the NiAl-B2 phase within the Ni/Al-units, whereas Peak II may be associated to the nucleation of the HEAF-B2 phase within the internal HEAF-unit. These two peaks apparently merge in the FSC scan at β = 50000 K/s. In this case, the exothermic event is not used for any quantitative analysis, because the sudden enthalpy release did not fully comply with the 'null-principle' used in power-compensated DSC during the reaction. A reason might have been that the thermal gradient within the sample might be non-negligible for such high rate. Yet, it can be stated that the range of applied heating rates was sufficient to observe the change in the mechanism from a multistep reaction to an explosive run-away reaction. The overall exothermic event for the FSC scan at 25000 K/s is sharp (T_{end}-T_{onset} = 90 K) and the overall heat of reaction is (-312 ± 56) J/g, or (-15.0 ± 2.7) kJ/mol, which is only 1/4 of that observed at 100 K/s, but large enough for the formation of the B2-structure as a whole in agreement with ref. [29]. These observations point towards a reaction of the multilayer composite as a whole when ultrafast rates are applied into a homogeneous B2-phase without the formation of intermediate phases that would require long-range diffusion.

5. Conclusions

In conclusion, the following points are observed in this study:

(1) A single phase B2-nanostructured AlCoCrFeNi HEAF was successfully synthesized via a combustion synthesis method using the SHS reaction that takes place in Ni/Al multilayers as a heat source. Depending on the design and placement of the NiAl layers, various nanocrystalline structures can be achieved, and the gradient-grain size structure is correlated to the heat fluxes generated from Ni-Al exothermic reaction.

(2) Periodic ripples as topological features are observed on reacted double stack Ni/Al-HEAF composites, whereas curtain-like features are found on triple stack Ni/Al-HEAF-Ni/Al composites. Depending on the stacking design, various

nanocrystalline structures can be achieved, and the gradient-grain size structure is correlated to the heat fluxes generated from Ni/Al exothermic reaction.

(3) A fast scanning calorimetry (FSC) study using a chip-calorimeter revealed that when the triple stack Ni/Al–HEAF–Ni/Al composite is scanned with a flash rate of 25000 K/s or greater a thermal explosion occurs at moderately low temperature of ~ 700 K via a sharp double-peak exothermic event. This reaction resembles that observed in electrical sparks ignited films, where the multistep phase sequence that is observed during slow annealing is kinetically suppressed altogether, and instead the polymorphic transformation into a homogeneous B2-structure takes place. A detailed kinetic analysis provided values for the activation energies of each observed exothermic reaction.

Declaration of Competing Interest

The authors declare that they have no known competing financial interests or personal relationships that could have appeared to influence the work reported in this paper.

Acknowledgments

Data availability

The raw data required to reproduce these findings are available to download from https://doi.org/10.5281/zenodo.4623001. The processed data required to reproduce these findings are available to download from https://doi.org/10.5281/zenodo.4623001.

References

[1] D.B. Miracle, O.N. Senkov, A critical review of high entropy alloys and related concepts, Acta Mater. 122 (2017) 448–511, https://doi.org/10.1016/j.actamat.2016.08.081.

[2] Y. Zhang, T.T. Zuo, Z. Tang, M.C. Gao, K.A. Dahmen, P.K. Liaw, Z.P. Lu, Microstructures and properties of high-entropy alloys, Prog. Mater Sci. 61 (2014) 1–93, https://doi.org/10.1016/j.pmatsci.2013.10.001.

[3] J.-W. Yeh, Physical Metallurgy of High-Entropy Alloys, JOM 67 (10) (2015) 2254–2261, https://doi.org/10.1007/s11837-015-1583-5.

[4] M.A. Tunes, V.M. Vishnyakov, Microstructural origins of the high mechanical damage tolerance of NbTaMoW refractory high-entropy alloy thin films, Mater. Des. 170 (2019), https://doi.org/10.1016/j.matdes.2019.107692 107692.

[5] W. Li, P. Liu, P.K. Liaw, Microstructures and properties of high-entropy alloy films and coatings: a review, Mater. Res. Lett. 6 (4) (2018) 199–229, https://doi.org/10.1080/21663831.2018.1434248.

[6] P.H. Mayrhofer, A. Kirnbauer, P. Ertelthaler, C.M. Koller, High-entropy ceramic thin films; A case study on transition metal diborides, Scripta Mater. 149 (2018) 93–97, https://doi.org/10.1016/j.scriptamat.2018.02.008.

[7] Y. Qiu, S. Thomas, D. Fabijanic, A.J. Barlow, H.L. Fraser, N. Birbilis, Microstructural evolution, electrochemical and corrosion properties of Al CoCrFeNiTi high entropy alloys, Mater. Des. 170 (2019), https://doi.org/10.1016/j.matdes.2019.107698.

[8] R. Grieseler, T. Kups, M. Wilke, M. Hopfeld, P. Schaaf, Formation of Ti2AlN nanolaminate films by multilayer-deposition and subsequent rapid thermal annealing, Mater. Lett. 82 (2012) 74–77, https://doi.org/10.1016/j.matlet.2012.05.055.

[9] R. Grieseler, F. Theska, T. Stürzel, B. Hähnlein, M. Stubenrauch, M. Hopfeld, T. Kups, J. Pezoldt, P. Schaaf, Elastic properties of nanolaminar Cr2AlC films and beams determined by in-situ scanning electron microscope bending tests, Thin Solid Films 604 (2016) 85–89, https://doi.org/10.1016/j.tsf.2016.03.026.

[10] M. Hopfeld, R. Grieseler, T. Kups, M. Wilke, P. Schaaf, Thin Film Synthesis of Ti3SiC2by Rapid Thermal Processing of Magnetron-Sputtered Ti-C-Si Multilayer Systems, Adv. Eng. Mater. 15 (4) (2013) 269–275, https://doi.org/10.1002/adem.201200180.

[11] Y.P. Cai, G.J. Wang, Y.J. Ma, Z.H. Cao, X.K. Meng, High hardness dual-phase high entropy alloy thin films produced by interface alloying, Scr. Mater. 162 (2019) 281–285, https://doi.org/10.1016/j.scriptamat.2018.11.004.

[12] K.B. Zhang, Z.Y. Fu, J.Y. Zhang, J. Shi, W.M. Wang, H. Wang, Y.C. Wang, Q.J. Zhang, Annealing on the structure and properties evolution of the CoCrFeNiCuAl high-entropy alloy, J. Alloy. Compd. 502 (2) (2010) 295–299, https://doi.org/10.1016/j.jallcom.2009.11.104.

[13] S. Singh, N. Wanderka, K. Kiefer, K. Siemensmeyer, J. Banhart, Effect of decomposition of the Cr-Fe-Co rich phase of AlCoCrCuFeNi high entropy alloy on magnetic properties, Ultramicroscopy 111 (6) (2011) 619–622, https://doi.org/10.1016/j.ultramic.2010.12.001.

[14] A. Wang, M.O. Ramirez, M. Caplovicova, V. Vretenar, J. Boettcher, M. Hopfeld, T. Kups, D. Flock, P. Schaaf, Formation of CuCrCoFeNiO high entropy alloy thin films by rapid thermal processing of Cu/CrNiO/FeCo multilayers, Surf. Coat. Technol. 405 (2021), https://doi.org/10.1016/j.surfcoat.2020.126563 126563.

[15] K. Rzyman, Z. Moser, Calorimetric studies of the enthalpies of formation of Al3Ni2, AlNi and AlNi3, Prog. Mater Sci. 49 (3–4) (2004) 581–606, https://doi.org/10.1016/j.pmatsci.2003.08.001.

[16] D.P. Adams, Reactive multilayers fabricated by vapor deposition: A critical review, Thin Solid Films 576 (2015) 98–128, https://doi.org/10.1016/j.tsf.2014.09.042.

[17] K.J. Blobaum, D. Van Heerden, A.J. Gavens, T.P. Weihs, Al/Ni formation reactions: characterization of the metastable Al9Ni2 phase and analysis of its formation, Acta Mater. 51 (13) (2003) 3871–3884, https://doi.org/10.1016/s1359-6454(03)00211-8.

[18] F.Z. Chrifi-Alaoui, M. Nassik, K. Mahdouk, J.C. Gachon, Enthalpies of formation of the Al–Ni intermetallic compounds, J. Alloy. Compd. 364 (1–2) (2004) 121–126, https://doi.org/10.1016/s0925-8388(03)00493-6.

[19] A.S. Edelstein, R.K. Everett, G.Y. Richardson, S.B. Qadri, E.I. Altman, J.C. Foley, J.H. Perepezko, Intermetallic phase formation during annealing of Al/Ni multilayers, J. Appl. Phys. 76 (12) (1994) 7850–7859, https://doi.org/10.1063/1.357893.

[20] R. Knepper, G. Fritz, T.P. Weihs, Controlling the shape of Al/Ni multilayer foils using variations in stress, J. Mater. Res. 23 (7) (2011) 2009–2016, https://doi.org/10.1557/jmr.2008.0247.

[21] R. Knepper, M.R. Snyder, G. Fritz, K. Fisher, O.M. Knio, T.P. Weihs, Effect of varying bilayer spacing distribution on reaction heat and velocity in reactive Al/Ni multilayers, J. Appl. Phys. 105 (8) (2009), https://doi.org/10.1063/1.3087490 083504.

[22] K.V. Manukyan, B.A. Mason, L.J. Groven, Y.-C. Lin, M. Cherukara, S.F. Son, A. Strachan, A.S. Mukasyan, Tailored Reactivity of Ni+Al Nanocomposites: Microstructural Correlations, J. Phys. Chem. C 116 (39) (2012) 21027–21038, https://doi.org/10.1021/jp303407e.

[23] C. Pauly, K. Woll, I. Gallino, M. Stüber, H. Leiste, R. Busch, F. Mücklich, Ignition in ternary Ru/Al-based reactive multilayers—Effects of chemistry and stacking sequence, J. Appl. Phys. 124 (19) (2018), https://doi.org/10.1063/1.5046452 195301.

[24] J.C. Trenkle, L.J. Koerner, M.W. Tate, S.M. Gruner, T.P. Weihs, T.C. Hufnagel, Phase transformations during rapid heating of Al/Ni multilayer foils, Appl. Phys. Lett. 93 (8) (2008), https://doi.org/10.1063/1.2975830 081903.

[25] Y.-F. Kao, T.-J. Chen, S.-K. Chen, J.-W. Yeh, Microstructure and mechanical property of as-cast, -homogenized, and -deformed AlxCoCrFeNi (0≤x≤2) high-entropy alloys, J. Alloy. Compd. 488 (1) (2009) 57–64, https://doi.org/10.1016/j.jallcom.2009.08.090.

[26] W.-R. Wang, W.-L. Wang, J.-W. Yeh, Phases, microstructure and mechanical properties of AlxCoCrFeNi high-entropy alloys at elevated temperatures, J. Alloy. Compd. 589 (2014) 143–152, https://doi.org/10.1016/j.jallcom.2013.11.084.

[27] C. Zhang, F. Zhang, H. Diao, M.C. Gao, Z. Tang, J.D. Poplawsky, P.K. Liaw, Understanding phase stability of Al-Co-Cr-Fe-Ni high entropy alloys, Mater. Des. 109 (2016) 425–433, https://doi.org/10.1016/j.matdes.2016.07.073.

[28] O. Stryzhyboroda, V.T. Witusiewicz, S. Gein, D. Röhrens, U. Hecht, Phase Equilibria in the Al–Co–Cr–Fe–Ni High Entropy Alloy System: Thermodynamic Description and Experimental Study, Front. Mater. 7 (270) (2020), https://doi.org/10.3389/fmats.2020.00270.

[29] C. Li, M. Zhao, J.C. Li, Q. Jiang, B2 structure of high-entropy alloys with addition of Al, J. Appl. Phys. 104 (11) (2008), https://doi.org/10.1063/1.3032900 113504.

[30] S. Sen, M. Lake, R. Grieseler, P. Schaaf, Effects of multilayer arrangement in ternary reactive film on self-propagating reaction properties, Surf. Coat. Technol. 327 (2017) 25–31, https://doi.org/10.1016/j.surfcoat.2017.07.065.

[31] S. Sen, M. Lake, N. Kroppen, P. Farber, J. Wilden, P. Schaaf, Self-propagating exothermic reaction analysis in Ti/Al reactive films using experiments and computational fluid dynamics simulation, Appl. Surf. Sci. 396 (2017) 1490–1498, https://doi.org/10.1016/j.apsusc.2016.11.197.

[32] S. Sen, M. Lake, J. Wilden, P. Schaaf, Synthesis and characterization of Ti/Al reactive multilayer films with various molar ratios, Thin Solid Films 631 (2017) 99–105, https://doi.org/10.1016/j.tsf.2017.04.012.

[33] S. Sen, M. Lake, P. Schaaf, Experimental investigation of high temperature oxidation during self-propagating reaction in Zr/Al reactive multilayer films, Surf. Coat. Technol. 340 (2018) 66–73, https://doi.org/10.1016/j.surfcoat.2018.02.014.

[34] G. Abadias, E. Chason, J. Keckes, M. Sebastiani, G.B. Thompson, E. Barthel, G.L. Doll, C.E. Murray, C.H. Stoessel, L. Martinu, Review Article: Stress in thin films and coatings: Current status, challenges, and prospects, J. Vacuum Sci. Technol. A: Vacuum, Surfaces, Films 36 (2) (2018), https://doi.org/10.1116/1.5011790.

[35] X. Monnier, D. Cangialosi, B. Ruta, R. Busch, I. Gallino, Vitrification decoupling from alpha-relaxation in a metallic glass, Sci. Adv. 6 (17) (2020) eaay1454, https://doi.org/10.1126/sciadv.aay1454.

[36] S. Gates-Rector, T. Blanton, The Powder Diffraction File: a quality materials characterization database, Powder Diffr. 34 (4) (2019) 352–360, https://doi.org/10.1017/s0885715619000812.

[37] M. Vaidya, A. Prasad, A. Parakh, B.S. Murty, Influence of sequence of elemental addition on phase evolution in nanocrystalline AlCoCrFeNi: Novel approach to alloy synthesis using mechanical alloying, Mater. Des. 126 (2017) 37–46, https://doi.org/10.1016/j.matdes.2017.04.027.

[38] G.-J. Cheng, B. Gault, C.-Y. Huang, C.-Y. Huang, H.-W. Yen, Warm ductility enhanced by austenite reversion in ultrafine-grained duplex steel, Acta Mater. 148 (2018) 344–354, https://doi.org/10.1016/j.actamat.2018.01.060.

[39] J.C. Trenkle, J. Wang, T.P. Weihs, T.C. Hufnagel, Microstructural study of an oscillatory formation reaction in nanostructured reactive multilayer foils, Appl. Phys. Lett. 87 (15) (2005), https://doi.org/10.1063/1.2099544 153108.

[40] H.E. Kissinger, Reaction Kinetics in Differential Thermal Analysis, Anal. Chem. 29 (11) (2002) 1702–1706, https://doi.org/10.1021/ac60131a045.

[41] L. Battezzati, P. Pappalepore, F. Durbiano, I. Gallino, Solid state reactions in Al/ Ni alternate foils induced by cold rolling and annealing, Acta Mater. 47 (6) (1999) 1901–1914, https://doi.org/10.1016/s1359-6454(99)00040-3.

[42] J.-B. Sun, J.-G. Yao, J. Meng, S. Li, Y. Jiang, J. Wang, Surface energies and electronic properties of intermetallic compound B2-AgMg, Mod. Phys. Lett. B 33 (08) (2019) 1950097, https://doi.org/10.1142/s0217984919500970.

[43] N. Zhou, T. Hu, J. Luo, Grain boundary complexions in multicomponent alloys: Challenges and opportunities, Curr. Opin. Solid State Mater. Sci. 20 (5) (2016) 268–277, https://doi.org/10.1016/j.cossms.2016.05.001.

[44] M.-H. Tsai, K.-C. Chang, J.-H. Li, R.-C. Tsai, A.-H. Cheng, A second criterion for sigma phase formation in high-entropy alloys, Mater. Res. Lett. 4 (2) (2015) 90–95, https://doi.org/10.1080/21663831.2015.1121168.

[45] J. Hao, Y. Ma, Q. Wang, C. Zhang, C. Li, C. Dong, Q. Song, P.K. Liaw, Formation of cuboidal B2 nanoprecipitates and microstructural evolution in the body-centered-cubic Al0.7NiCoFe1.5Cr1.5 high-entropy alloy, J. Alloys Compounds 780 (2019) 408–421, https://doi.org/10.1016/j.jallcom.2018.11.381.

[46] Y. Shi, B. Yang, P.D. Rack, S. Guo, P.K. Liaw, Y. Zhao, High-throughput synthesis and corrosion behavior of sputter-deposited nanocrystalline Al (CoCrFeNi) 100- combinatorial high-entropy alloys, Mater. Des. 195 (2020), https://doi.org/10.1016/j.matdes.2020.109018.

[47] B.M. Clemens, R. Sinclair, Metastable Phase Formation in Thin Films and Multilayers, MRS Bull. 15 (2) (2013) 19–28, https://doi.org/10.1557/s0883769400060425.

[48] Q. Tang, Y. Huang, H. Cheng, X. Liao, T.G. Langdon, P. Dai, The effect of grain size on the annealing-induced phase transformation in an Al0·3CoCrFeNi high entropy alloy, Mater. Des. 105 (2016) 381–385, https://doi.org/10.1016/j.matdes.2016.05.079.

[49] F. He, Z. Wang, Y. Li, Q. Wu, J. Li, J. Wang, C.T. Liu, Kinetic ways of tailoring phases in high entropy alloys, Sci. Rep. 6 (1) (2016), https://doi.org/10.1038/srep34628.

[50] P. Wynblatt, D. Chatain, Anisotropy of segregation at grain boundaries and surfaces, Metall. Mater. Trans. A 37 (9) (2006) 2595–2620, https://doi.org/10.1007/BF02586096.

[51] R. Pretorius, R. de Reus, A.M. Vredenberg, F.W. Saris, Use of the effective heat of formation rule for predicting phase formation sequence in Al-Ni systems, Mater. Lett. 9 (12) (1990) 494–499, https://doi.org/10.1016/0167-577x(90)90094-3.

[52] H. Aboulfadl, I. Gallino, R. Busch, F. Mücklich, Atomic scale analysis of phase formation and diffusion kinetics in Ag/Al multilayer thin films, J. Appl. Phys. 120 (19) (2016), https://doi.org/10.1063/1.4968013 195306.

[53] K. Rzyman, Z. Moser, R.E. Watson, M. Weinert, Enthalpies of formation of AlNi: Experiment versus theory, J. Phase Equilibria 19 (2) (1998) 106–111, https://doi.org/10.1361/105497198770342562.

[54] Y. Du, N. Clavaguera, Thermodynamic assessment of the Al-Ni system, J. Alloy. Compd. 237 (1–2) (1996) 20–32, https://doi.org/10.1016/0925-8388(95)02085-3.

[55] M.D. Grapes, T. LaGrange, K. Woll, B.W. Reed, G.H. Campbell, D.A. LaVan, T.P. Weihs, In situ transmission electron microscopy investigation of the interfacial reaction between Ni and Al during rapid heating in a nanocalorimeter, APL Mater. 2 (11) (2014), https://doi.org/10.1063/1.4900818 116102.

[56] T. Neuhauser, G. Tinti, H. Leiste, N. Casati, M. Stüber, K. Woll, Analysis of the reaction runaway in Al/Ni multilayers with combined nanocalorimetry and time-resolved X-ray diffraction, Acta Mater. 195 (2020) 579–587, https://doi.org/10.1016/j.actamat.2020.05.035.

[57] Z. Li, Y. Xie, Y. Yuan, Y. Ji, V. Begeza, L. Cao, R. Hübner, L. Rebohle, M. Helm, K. Nielsch, S. Prucnal, S. Zhou, Phase Selection in Mn–Si Alloys by Fast Solid-State Reaction with Enhanced Skyrmion Stability, Adv. Funct. Mater. (2021), https://doi.org/10.1002/adfm.202009723.

[58] T. Neuhauser, G. Tinti, H. Leiste, N. Casati, S. Ulrich, M. Stüber, K. Woll, The role of two-stage phase formation for the solid-state runaway reaction in Al/Ni reactive multilayers, Appl. Phys. Lett. 117 (1) (2020), https://doi.org/10.1063/5.0011338.

[59] P. Yi, D. Ruan, T.P. Weihs, M.L. Falk, Predicting the Rate of Homogeneous Intermetallic Nucleation within Steep Composition Gradients, J. Phys. Chem. C 124 (43) (2020) 23807–23814, https://doi.org/10.1021/acs.jpcc.0c08591.